Electronic Supplementary Material (ESI) for Chemical Science.
This journal is © The Royal Society of Chemistry 2024

Electronic Supporting information

Critical assessment on the interactions between ct-DNA and choline based magnetic ionic liquids: Evidences of compaction

Kiran Devi Tulsiyan [a,b], Saroj Kumar Panda [c], Malay Kumar Rana [c*] and Himansu S. Biswal [a,b*]

[a]School of Chemical Sciences, National Institute of Science Education and Research (NISER), PO- Bhimpur-Padanpur, Via-Jatni, District- Khurda, PIN - 752050, Bhubaneswar, India

[b]Homi Bhabha National Institute, Training School Complex, Anushakti Nagar, Mumbai 400094, India

[c]Department of Chemical Sciences, Indian Institute of Science Education and Research (IISER) Berhampur, Odisha-760010, India.

* Corresponding Author's E-mail: himansu@niser.ac.in, Phone No: - +91-674-2494 185/186

Table of Contents

Experimental Section:

Materials:

Chemicals like Choline chloride, metal salts ($FeCl_3$, $MnCl_2$), DNA from calf thymus and the fluorescence probe - DAPI, are from Sigma and used without further purification. Phosphate buffer (1M, pH 7.4) and the fluorescence dye - Ethidium bromide (EB) is from G Bioscience. Synthesis of ionic liquids (ILs) are according to the previous report. The purity analysis of synthesized molecules was characterized using NMR (1H and 13C) (Figure S1-4) and EPR (Figure S5) spectroscopy. UV/Vis absorbance measurement at 260 and 280 nm gives a ratio of 1.8, which confirms the purity of DNA. All the sample preparation and experimental measurements were done using deionized Milli Q water.

Instrumentation and Methods:

For steady-state absorption measurement, we use a UV/Vis spectrometer from Agilent Cary; for the fluorescence spectral measurement, a spectro-fluorimeter from PerkinElmer; and for circular dichroism (CD) measurements, a spectro-polarimeter from JASCO J-1500. Spectral accumulations are an average of three scans. Measurements of the time-resolved fluorescence properties use an Edinburgh.

All sample preparations for recording steady-state absorption, emission, time-resolved emission, and CD are in 20 mM aqueous phosphate buffer solution of pH 7.4. These measurements are in a quartz cuvette of 10 mm path length. The UV melting measurement uses a fixed wavelength of 260 nm with gradual recording from 40 to 95 ^{o}C. For the time-resolved measurements, 445 laser was used as the excitation source. The obtained IRF from the ludox solution is 120 ps. Isothermal titration calorimetry (ITC) measurement uses a MicroCal ITC-200 calorimeter at 25 ^{o}C. The recordings are with a sample cell containing 200 µL of 50 µM DNA in phosphate buffer and titration against 50 mM injections of ChMILs. A total of 19 injections are used from a 40 µL rotating syringe into the sample cell. In each titration, an injection volume of 2 µL at an interval of 120 s. The field emission scanning electron microscope (FE-SEM) images of DNA and DNA-Gua-IL systems were taken from a ZEISS, Ultra Plus, where all the samples were prepared by drop casting the solution in silicon wafers.

Fluorescence correlation spectral measurements use a time-resolved confocal microscope from PicoQuant Micro-time 200. The excitation source uses a pulsed diode laser with a wavelength of 403 nm. Laser focus on the sample uses a water immersion objective. The experimental

recordings use a laser power of 10 μW in 20 mM phosphate buffer solution containing 150 nM DAPI and 50 μM DNA. The observed correlation data was fitted using the equation for simple diffusion along with intersystem crossing is as follows:

$$G(\tau) = \frac{1}{N}(1 + \frac{\tau}{\tau_D})^{-1}(1 + \frac{\tau}{\kappa^2\tau_D})^{-1/2}$$

$$G(\tau) = \frac{1 - T + Te^{-\tau/\tau_{tr}}}{N(1-T)}(1 + \frac{\tau}{\tau_D})^{-1}(1 + \frac{\tau}{\kappa^2\tau_D})^{-1/2}$$

Here, τ_D is the diffusion time, N represents the number of molecules in the observation volume, and κ is the structure parameter defined as $\kappa = (\omega_z/\omega_{xy})$ in which ω_z and ω_{xy} are the longitudinal and transverse radii of the observation volume, respectively.

Computational methods:

Methodology:

In this work, the AMBER99SB[1] force field was used to mimic the interatomic interactions of $[Chl]^+$ ions. For $[MnCl_4]^{2-}$ and $[FeCl_4]^-$, the Panteva and York fine-tuned divalent cation parameters[2] and the universal force field (UFF) described by Rappe *et al.*[3] were used, respectively. By prior benchmark assessment investigations, the Amber99sb force field has demonstrated heightened accuracy and compatibility in the realm of biomolecular simulations.[4-6] In ESI, **Table S1** provides all force field parameters employed in this study. Simulations were performed for two systems, namely (i) DNA-[Ch][Fe] IL in water and (ii) DNA-$[Ch]_2$[Mn] in water.

Molecular docking:

The molecular docking calculations for the aforementioned complexes were conducted employing the AutoDock Vina package.[7-10] The ct-DNA dodecamer, identified by the PDB accession 1BNA, was obtained from the RCSB Protein Data Bank[11], with subsequent removal of extraneous water molecules and other entities. The ChMILs were subjected to docking within a predefined grid box (X = 15.2 Å, Y = 19.9 Å, Z = 8.9 Å) established around the DNA structure. Ten binding poses were generated for each complex, guided by the binding affinity of the complexes with the DNA dodecamer. Clusters featuring the most favorable binding poses were subsequently singled out for in-depth analysis. BIOVIA Discovery Studio

Visualizer 4.5[12] was utilized to comprehensively explore the dynamic interaction between the docked complexes and DNA. This facilitated a meticulous examination of binding modes and the discernment of pivotal interactions contributing to the binding affinity.

Simulations details:

For the molecular dynamic simulation of DNA in magnetic ionic liquids (ILs), we used the Gromacs 2021 package[13]. Once the topology was generated based on the above-mentioned force field parameters, the DNA molecule was kept in a cubic simulation box with a minimum of 10 nm distance from its surface and filled with the simple point charge (SPC) water molecules[14]. Specifically, the docked pose obtained serves as the basis for generating a system composition, 1:30. Around the docked complex, 29 more MIL molecules were inserted into the simulation box. Consistent with the experimental composition, the ratio of DNA to [Chl][$FeCl_4$] or $[Chl]_2[MnCl_4]$ in the box was set at 1:30. Requisite counterions were added to make every system electrically neutral. Having accomplished energy minimization with the steepest descent integrator for 5000 steps under a force convergence of < 1000 kcal. mol^{-1}. nm^{-1}, we ran MD simulations.

First, the canonical (NVT) and isothermal-isobaric (NPT) ensembles were used to equilibrate each system for 5 ns. We employed the Parrinello-Rahman pressure and Berendsen temperature controllers during equilibration to maintain 1 bar pressure and 300 K temperature, respectively. With a Fourier grid spacing of 0.12 nm, the long-range Coulomb interactions were treated using the particle mesh Ewald (PME) technique[15]. The short-range van der Waals interaction was modeled by the Lennard-Jones potential function with a cut-off distance of 1 nm. The linear constraint solver (LINCS)[16] method was used to limit all bond vibrations.

After equilibration, two systems were subjected to 1 μs production runs, with the system's coordinates being stored at an interval of 10 ps. As in previous studies[17, 18], post-MD analyses, including root-mean-square-deviation (RMSD), solvent accessible surface area (SASA), principal component analysis (PCA), radial distribution function (RDF), and H-bonds, were performed using MD trajectories. Applying the MM-PBSA method[19], binding free energies for the two systems were computed.

The MM-PBSA method[20] was used to calculate the binding free energy of protein-ligand complexes. The studies suggest that the goodness of the agreement between experimentally determined binding affinities and those computed with MM-PBSA[21]. Although MM-PBSA proved its strengths in many drug designs and macromolecular analyses, the studies also

revealed weaknesses of the method. Sources of uncertainty in the MM-PBSA method encompass challenges in predicting solute entropies, estimating solvation free energies for charged groups situated in buried environments, addressing conformational sampling intricacies, and making precise parameter choices, including the determination of radii for solvation free energy calculation and the selection of the dielectric constant for the solute. The computation of the entropy term poses a formidable challenge, frequently necessitating approximation through a normal mode method employing a limited number of chosen snapshots. In such an approach, the configurational entropy derived from normal mode analysis is frequently excluded in the hierarchical ranking of relative binding affinities, as its incorporation often fails to yield substantial enhancement in concordance with experimental observations. The normal-mode entropy is beset by computational expense and a deficiency in providing insights into conformational entropy. Regrettably, alternative methodologies fail to yield converged results. Therefore, the term is often omitted.[22-25]

The MM-PBSA method is widely used for free energy calculation from the MD trajectory. A benchmarking study by Wang et al. in 2019 showed that MM-PBSA outperformed the Glide SP scoring function (success rate of 58.6%) and MMGBSA in most cases with an overall success rate of about 74%.[26]

The binding free energy (ΔG_{bind}) in a solvent medium was calculated as follows:

$$\Delta G_{bind} = G_{complex} - (G_{protein} + G_{ligand}),$$

where $G_{complex}$ is the total free energy of the protein-ligand complex; Gprotein and Gligand for the protein and ligand alone in a solvent, respectively.

Each free energy term G_p (p = protein, ligand, or complex) is a combination of the average molecular mechanics potential energy in the vacuum (E_{MM}) and solvation free energy (G_{solv}):

$$G_p = E_{MM} + G_{solv}.$$

EMM was calculated in the vacuum as follows:

$$E_{MM} = E_{bonded} + E_{non\text{-}bonded} = E_{bonded}\ (E_{int}) + E_{vdw} + E_{elec},$$

where E_{bonded} (or E_{int}) is the total bonded interaction, which includes bond, angle, dihedral, and improper interactions. Enon-bonded is the total non-bonded interaction consisting of both van der Waals (E_{vdw}) and electrostatic (E_{elec}) interactions. Ebonded is always taken as zero.

The solvation free energy (G_{solv}) was estimated as the sum of electrostatic solvation free energy (G_{polar}) and nonpolar solvation free energy ($G_{non\text{-}polar}$) as given below:

$G_{solv} = G_{polar} + G_{non\text{-}polar}$,

where Gpolar, the polar solvation energy, was determined using the Poisson-Boltzmann (PB) linear equation, and the nonpolar contribution, Gnon-polar, was estimated from the solvent-accessible surface area (SASA) as per the following equation:

Gnon-polar = γSASA + b,

where γ (a coefficient related to the surface tension of the solvent) = 0.02267 kJ/mol/Å^2 and b = 3.849 kJ/mol.

To quantify the affinity and binding strength between DNA and ILs, we estimated binding free energy (ΔG_{bind}) by taking the final 10 ns of MD trajectories.

Upon conducting post-molecular dynamics analyses, including root-mean-square deviation (RMSD), solvent accessible surface area (SASA), and others, it has been observed that all investigated systems exhibit convergence well before the designated simulation duration of 1 μs. Notably, conformational stability persists beyond the 400 ns mark, suggesting comprehensive coverage of simulation windows within this temporal domain.

The visualization of all simulation structures was facilitated through the utilization of VMD (Visual Molecular Dynamics) software[27], while the superimposition of structures was achieved employing UCSF Chimera[28], a molecular visualization and analysis tool.

Table S1. Force field parameters for $[Ch]^+$, $[FeCl4]^-$ and $[MnCl_4]^{2-}$ ions used in this work.

$[Ch]^+$ **Force field:** AMBER99SB[1]		
Atoms	**σ (nm)**	**ε (kJ/mol)**
N4	2.49951E-01	1.62122e+0
C3	3.39771E-01	4.51035E-01
OH	3.24287E-01	3.89112E-01
HO	5.37925E-02	1.96648E-02

HX	1.88746E-01	8.70272E-02
H1	2.42200E-01	8.70272E-02
$[FeCl_4]^-$ **Force field:** Universal Force Field (UFF)[3]		
Fe	2.08000E-01	0.560656
Cl	3.47000E-01	1.10876
$[MnCl_4]^{2-}$ **Force Field:** Panteva and York's fine-tuned divalent cation parameters[2]		
Mn	3.01123E-01	0.058576
Cl	3.47000E-01	1.10876

Bond parameters			
$[Ch]^+$			
Atom	**Atom**	**r_{eq} (nm)**	**K_b (kJ/mol.nm^2)**
1	2	1.5110E-01	1.8627E+05
1	3	1.5110E-01	1.8627E+05
1	4	1.5110E-01	1.8627E+05
1	5	1.5110E-01	1.8627E+05
2	16	1.0910E-01	3.2342E+05
2	17	1.0910E-01	3.2342E+05
2	18	1.0910E-01	3.2342E+05
3	13	1.0910E-01	3.2342E+05
3	14	1.0910E-01	3.2342E+05
3	15	1.0910E-01	3.2342E+05
4	19	1.0910E-01	3.2342E+05

4	20	1.0910E-01	3.2342E+05
4	21	1.0910E-01	3.2342E+05
5	6	1.5380E-01	1.9456E+05
5	9	1.0910E-01	3.2342E+05
5	10	1.0910E-01	3.2342E+05
6	7	1.4230E-01	2.4552E+05
6	11	1.0970E-01	3.1455E+05
6	12	1.0970E-01	3.1455E+05
7	8	9.7300E-02	4.7154E+05
1	2	1.5110E-01	1.8627E+05
1	3	1.5110E-01	1.8627E+05
1	4	1.5110E-01	1.8627E+05
1	5	1.5110E-01	1.8627E+05
2	16	1.0910E-01	3.2342E+05
2	17	1.0910E-01	3.2342E+05
2	18	1.0910E-01	3.2342E+05
$[FeCl_4]^-$			
Fe	Cl	0.22600	328.27664
$[MnCl_4]^{2-}$			
Mn	Cl	0.238974	328.27664

Angle parameters

$[Ch]^+$

Atom	**Atom**	**Atom**	**θ (deg)**	**K_θ (kJ.mol^{-1}.rad^{-2})**
1	2	1	1.08E+02	5.03E+02

1	2	1	1.08E+02	5.03E+02
1	2	1	1.08E+02	5.03E+02
1	3	1	1.08E+02	5.03E+02
1	3	1	1.08E+02	5.03E+02
1	3	1	1.08E+02	5.03E+02
1	4	1	1.08E+02	5.03E+02
1	4	1	1.08E+02	5.03E+02
1	4	1	1.08E+02	5.03E+02
1	5	1	1.14E+02	6.78E+02
1	5	1	1.08E+02	5.03E+02
1	5	1	1.08E+02	5.03E+02
2	1	1	1.10E+02	5.40E+02
2	1	1	1.10E+02	5.40E+02
2	1	1	1.10E+02	5.40E+02
3	1	1	1.10E+02	5.40E+02
3	1	1	1.10E+02	5.40E+02
4	1	1	1.10E+02	5.40E+02
5	6	1	1.10E+02	7.08E+02
5	6	1	1.10E+02	3.92E+02
5	6	1	1.10E+02	3.92E+02
6	5	1	1.11E+02	3.91E+02
6	5	1	1.11E+02	3.91E+02
6	7	1	1.07E+02	4.10E+02
7	6	1	1.10E+02	5.23E+02
7	6	1	1.10E+02	5.23E+02
9	5	1	1.10E+02	3.25E+02
11	6	1	1.08E+02	3.25E+02
13	3	1	1.10E+02	3.25E+02
13	3	1	1.10E+02	3.25E+02
14	3	1	1.10E+02	3.25E+02
16	2	1	1.10E+02	3.25E+02
16	2	1	1.10E+02	3.25E+02
17	2	1	1.10E+02	3.25E+02
19	4	1	1.10E+02	3.25E+02
19	4	1	1.10E+02	3.25E+02
20	4	1	1.10E+02	3.25E+02
22	23	1	1.08E+02	5.03E+02
22	23	1	1.08E+02	5.03E+02
22	23	1	1.08E+02	5.03E+02
22	24	1	1.08E+02	5.03E+02
22	24	1	1.08E+02	5.03E+02
22	24	1	1.08E+02	5.03E+02
22	25	1	1.08E+02	5.03E+02
22	25	1	1.08E+02	5.03E+02
22	25	1	1.08E+02	5.03E+02
22	26	1	1.14E+02	6.78E+02
22	26	1	1.08E+02	5.03E+02
22	26	1	1.08E+02	5.03E+02

23	22	1	1.10E+02	5.40E+02
23	22	1	1.10E+02	5.40E+02
23	22	1	1.10E+02	5.40E+02
24	22	1	1.10E+02	5.40E+02
24	22	1	1.10E+02	5.40E+02
25	22	1	1.10E+02	5.40E+02
26	27	1	1.10E+02	7.08E+02
26	27	1	1.10E+02	3.92E+02
26	27	1	1.10E+02	3.92E+02
27	26	1	1.11E+02	3.91E+02
27	26	1	1.11E+02	3.91E+02
27	28	1	1.07E+02	4.10E+02
28	27	1	1.10E+02	5.23E+02
28	27	1	1.10E+02	5.23E+02
30	26	1	1.10E+02	3.25E+02
32	27	1	1.08E+02	3.25E+02
34	24	1	1.10E+02	3.25E+02
34	24	1	1.10E+02	3.25E+02
35	24	1	1.10E+02	3.25E+02
37	23	1	1.10E+02	3.25E+02
37	23	1	1.10E+02	3.25E+02
38	23	1	1.10E+02	3.25E+02
40	25	1	1.10E+02	3.25E+02
40	25	1	1.10E+02	3.25E+02
41	25	1	1.10E+02	3.25E+02
43	44	1	1.09E+02	9.74E+02
43	44	1	1.09E+02	9.74E+02
43	44	1	1.09E+02	9.74E+02
45	44	1	1.09E+02	9.74E+02
46	44	1	1.09E+02	9.74E+02
45	44	1	1.09E+02	9.74E+02
34	24	1	1.10E+02	3.25E+02
35	24	1	1.10E+02	3.25E+02
37	23	1	1.10E+02	3.25E+02
37	23	1	1.10E+02	3.25E+02
$[FeCl_4]^-$				
22	24	23	1.09E+02	9.74E+02
22	24	25	1.09E+02	9.74E+02
22	24	26	1.09E+02	9.74E+02
23	24	25	1.09E+02	9.74E+02
25	24	26	1.09E+02	9.74E+02
23	24	26	1.09E+02	9.74E+02
$[MnCl_4]^{2-}$				
43	44	45	1.09E+02	9.74E+02
43	44	46	1.09E+02	9.74E+02
43	44	47	1.09E+02	9.74E+02
45	44	46	1.09E+02	9.74E+02
46	44	47	1.09E+02	9.74E+02

45	44	47	1.09E+02	9.74E+02

Table S2: The length and diameter of DNA in the [Ch][Fe] ionic liquid at different instants: 0, 200, 500, 700, and 1000 ns.

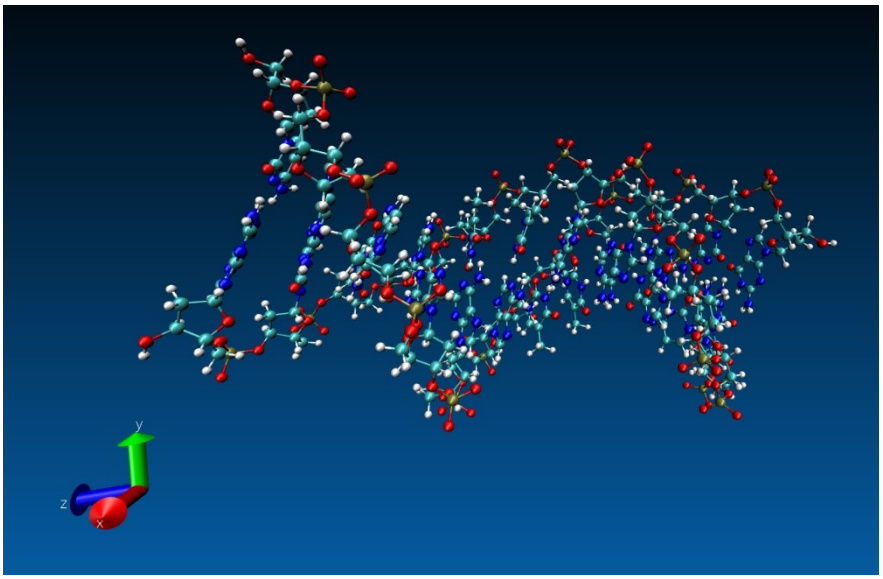

Time instant (ns)	Length (Å)	Diameter (Å)
0	43.6	27.2
200	41.9	34.2
500	40.5	38.7
700	45.9	30.8
1000	38.5	33.6

Table S3: The length and diameter of DNA in the $[Ch]_2[Mn]$ ionic liquid at different instants: 0, 200, 500, 700, and 1000 ns.

Time instants (ns)	Length (Å)	Diameter (Å)
0	44.5	26.9
200	47.5	26.2
500	40.8	32.9
700	39.5	32.9
1000	39.6	35.3

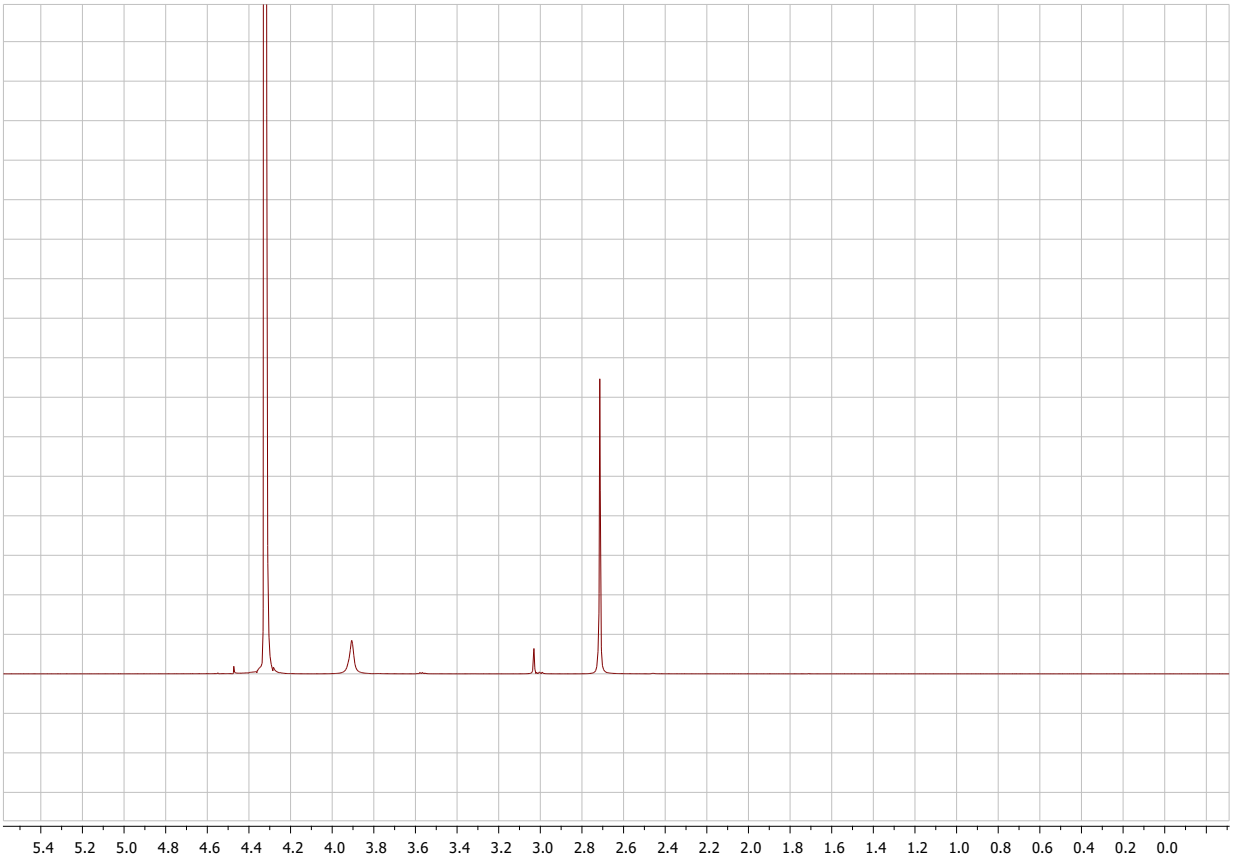

Figure S1. ^{1}H NMR spectra of [Ch][Fe] IL

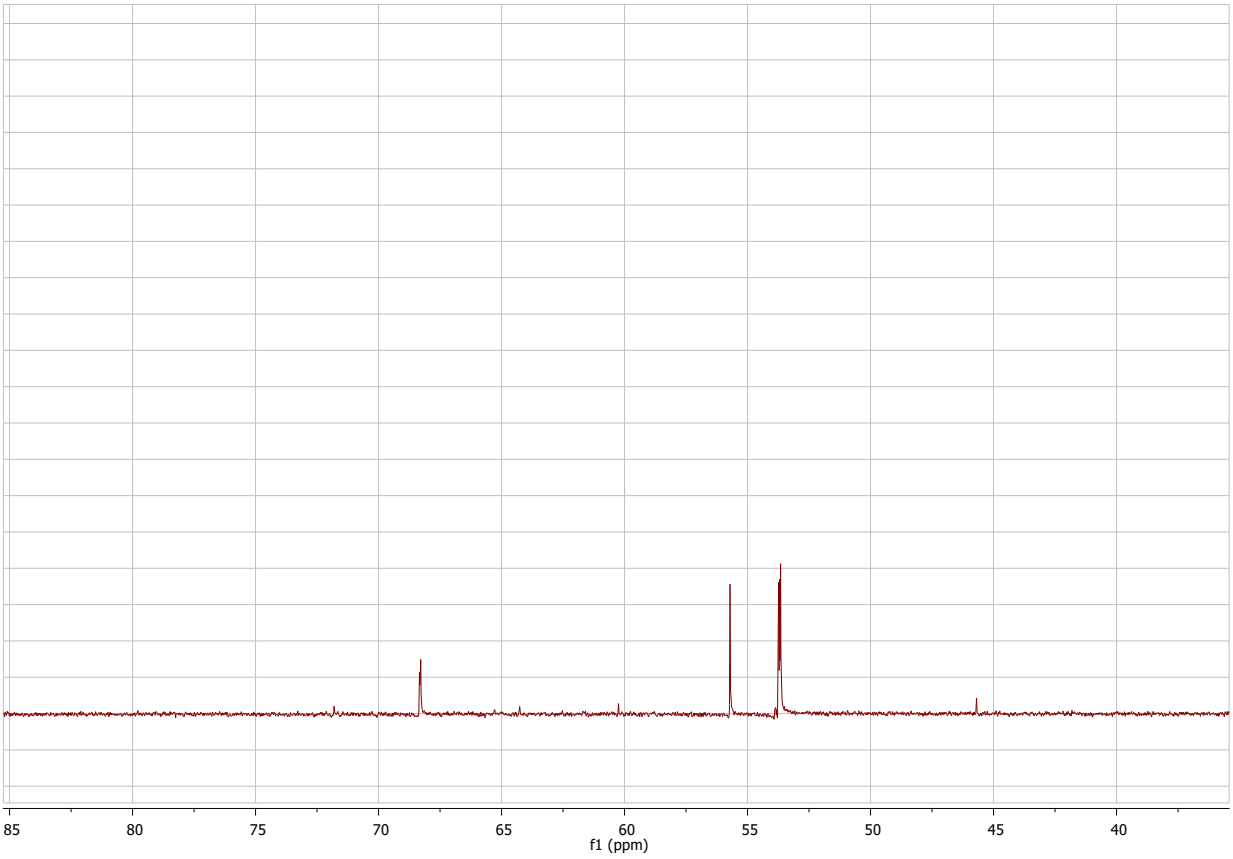

Figure S2. ^{13}C NMR spectra of [Ch][Fe] IL

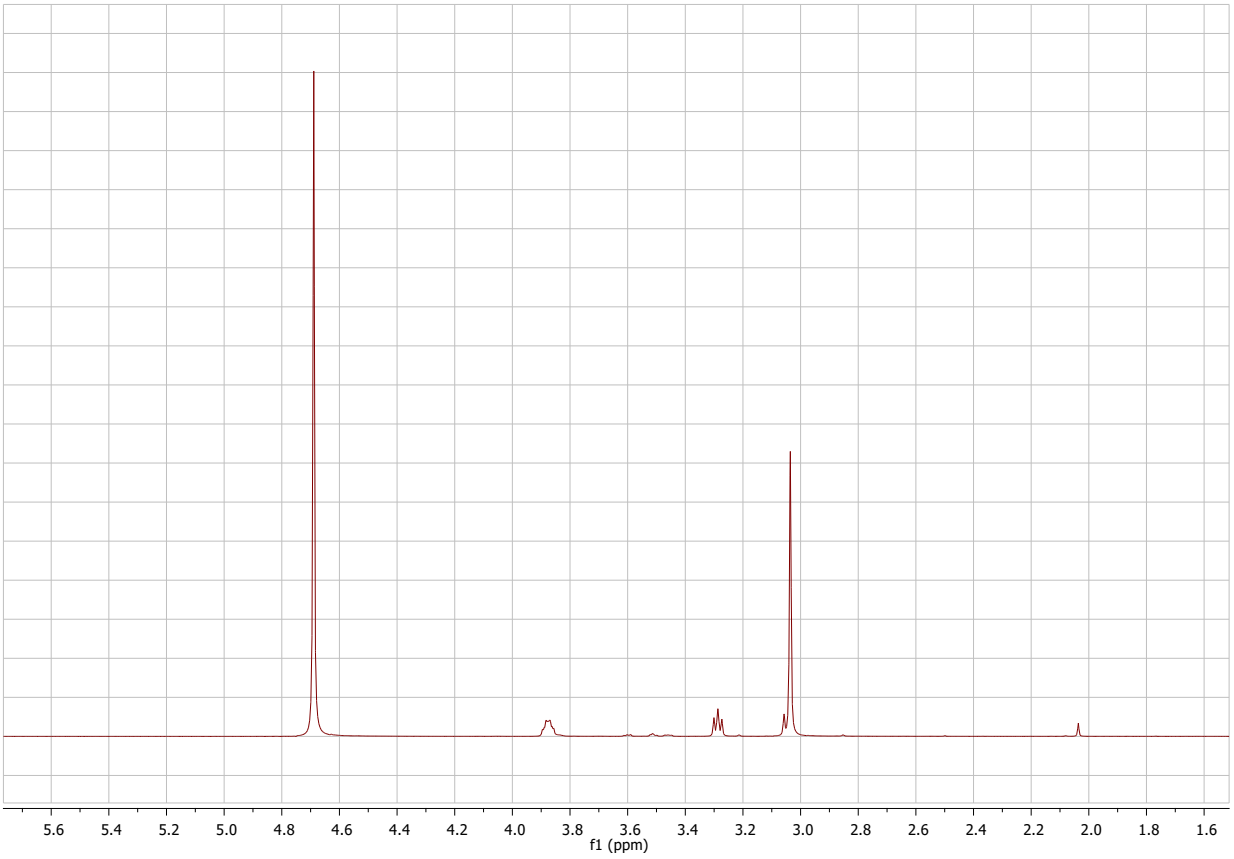

Figure S3. ^{1}H NMR spectra of $[Ch]_2[Mn]$ IL

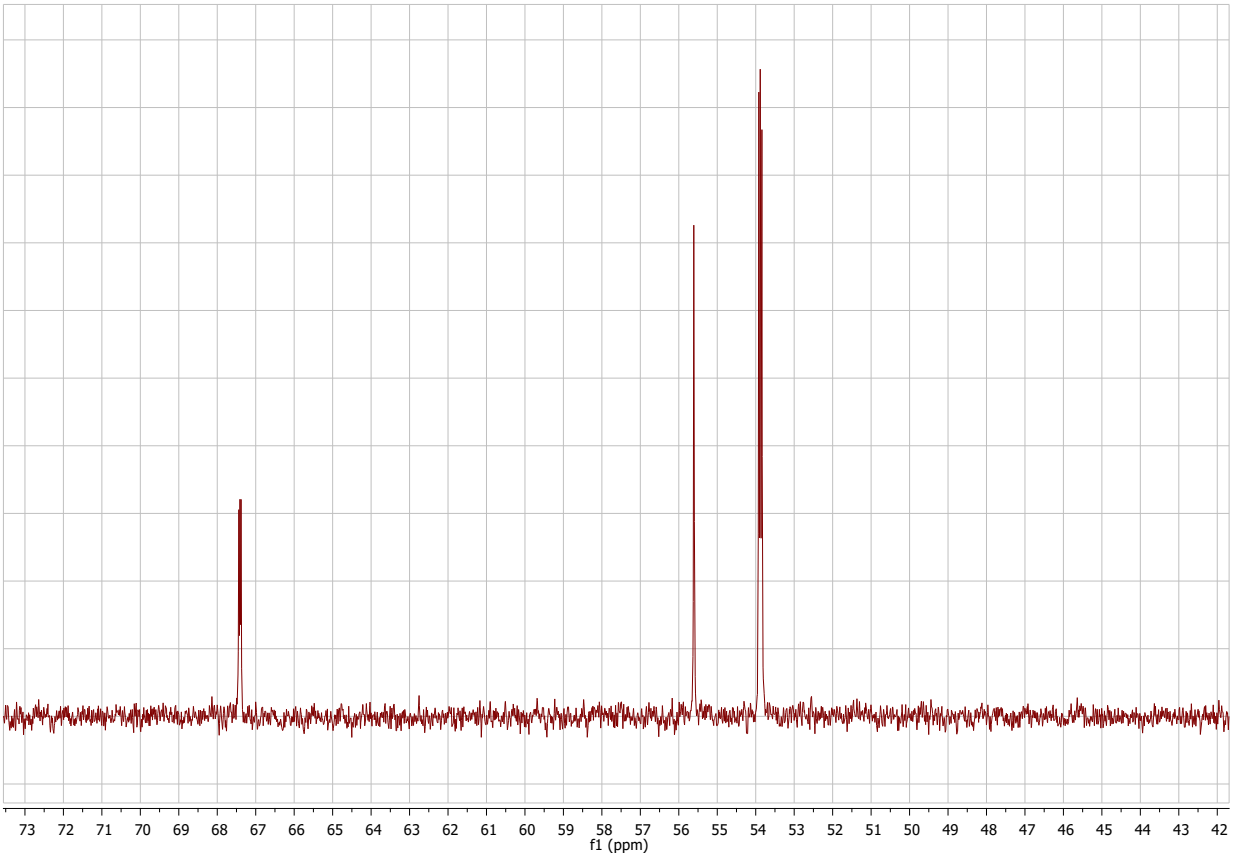

Figure S4. ^{13}C NMR spectra of $[Ch]_2[Mn]$ IL

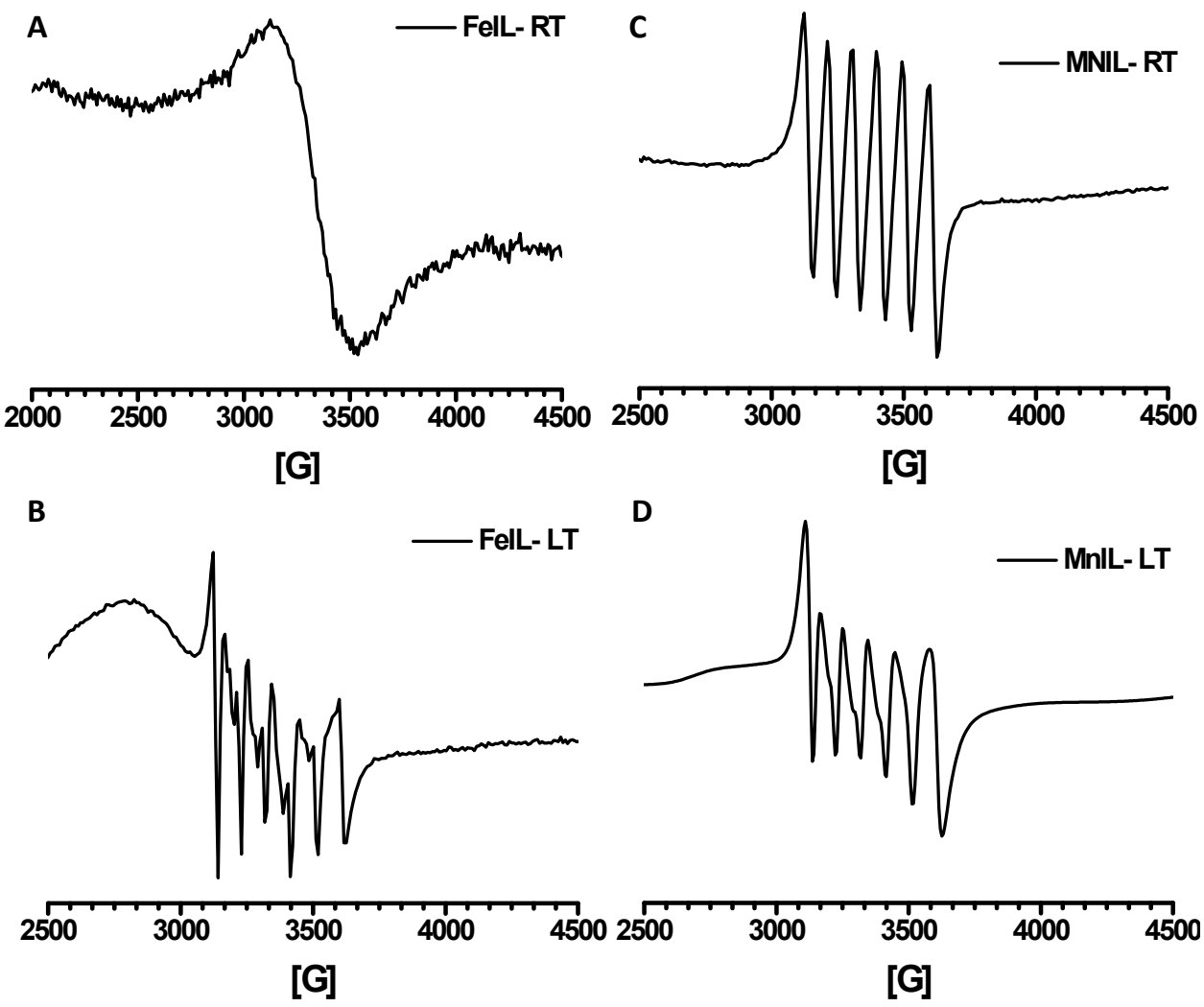

Figure S5. A) X-band EPR spectrum of [Ch][Fe] IL at room temperature in CH_3OH, B) X-band EPR spectrum of [Ch][Fe] IL at 100 K in CH_3OH, C) X-band EPR spectrum of $[Ch]_2[Mn]$ IL at room temperature in CH_3OH, D) X-band EPR spectrum of $[Ch]_2[Mn]$ IL at 100 K in CH_3OH.

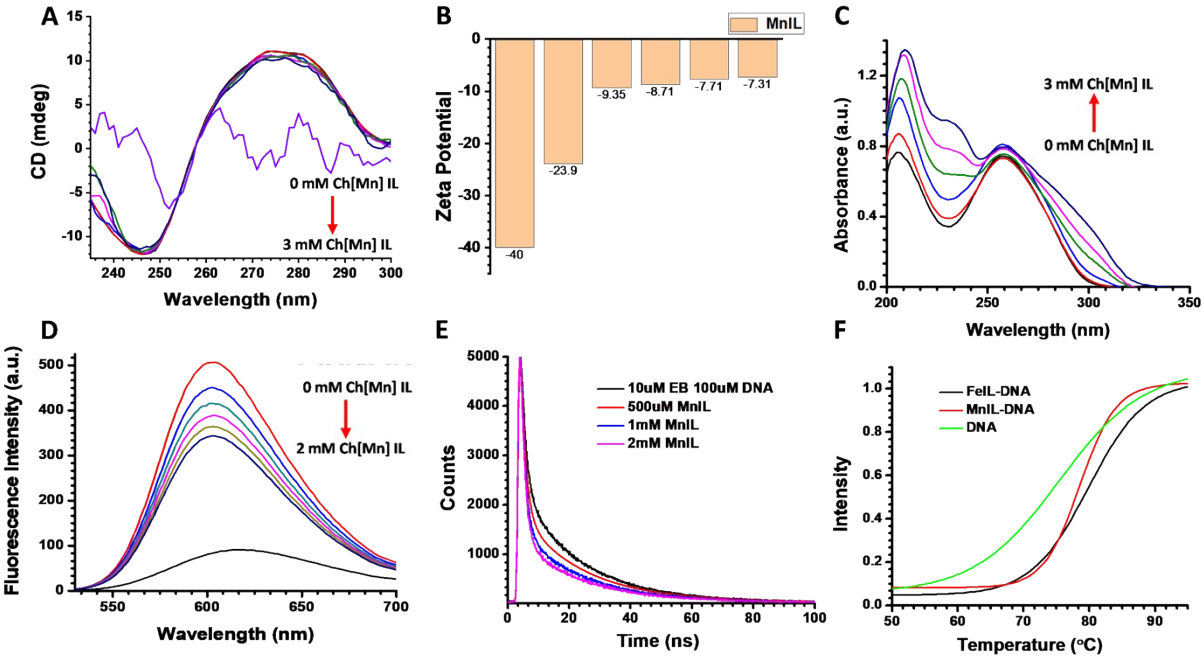

Figure S6. A) Circular dichroism spectra of 50 mM DNA in phosphate buffer (10mM, pH 7.0) and with increasing concentration of $[Ch]_2[Mn]$ upto 5mM B) Zeta potential of DNA in absence and presence of varying amount of $[Ch]_2[Mn]$ IL C) Absorption spectra of DNA in absence and presence of varying amount of $[Ch]_2[Mn]$ IL D) Emission spectra of free EB(10 µM), DNA bound EB(10 µM, 50 µM DNA) and on varying the amount of $[Ch]_2[Mn]$ ILs, E) Fluorescence decay profiles of EB-DNA in buffer and EB-DNA system in presence of $[Ch]_2[Mn]$ IL F) Melting curves of DNA in buffer, [Ch][Fe] IL, and $[Ch]_2[Mn]$ IL.

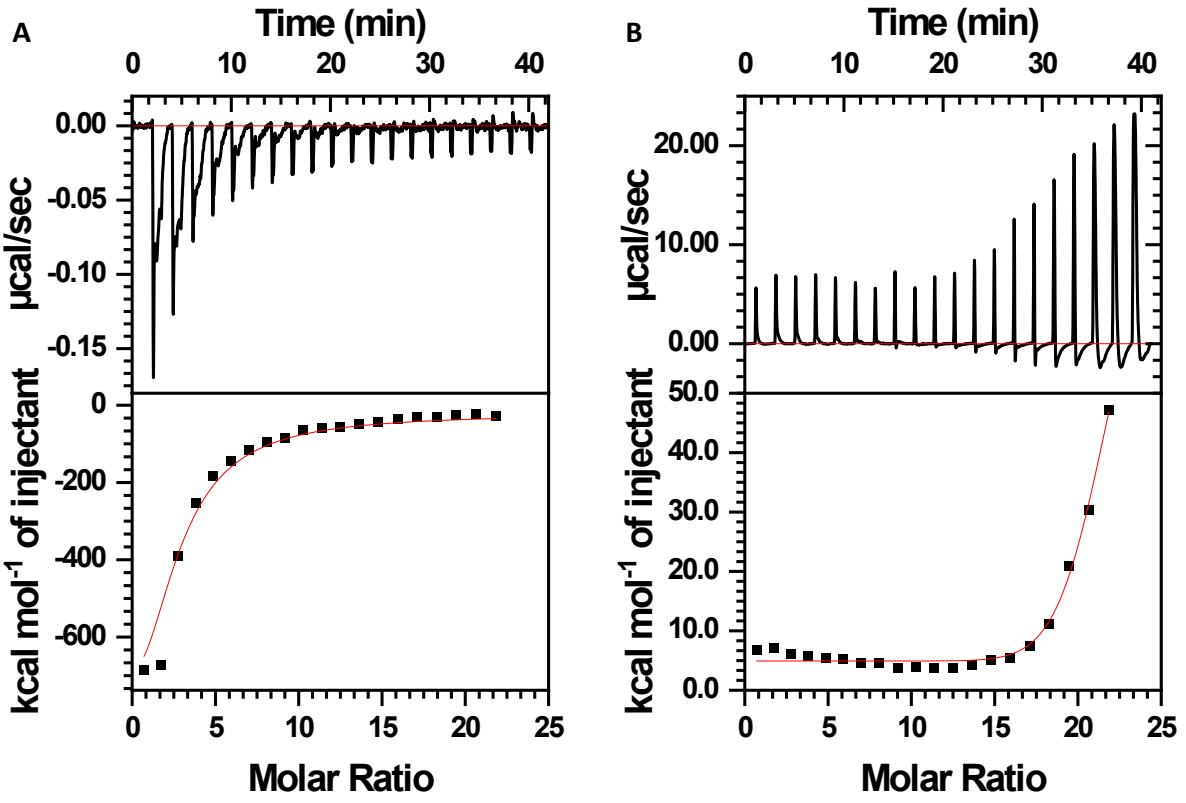

Figure S7. A) ITC isotherms of EB-DNA binding in buffer B) ITC isotherms of $[Ch]_2[Mn]$-DNA binding in buffer. Top part of both panels are obtained by converting the results into molar heats and plotted against the ligand to DNA molar ratio. Bottom part of both left and right panels are integrated data.

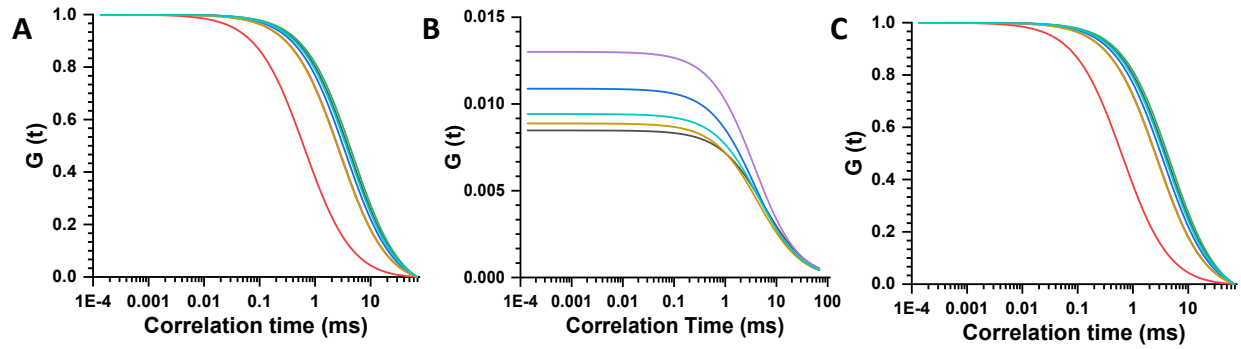

Figure S8. A) Normalised FCS data of DNA-DAPI complex in absence and presence of varying amount of [Ch][Fe] IL B) FCS data of DNA-DAPI complex in absence and presence of varying amount of $[Ch]_2[Mn]$ IL C) Normalised FCS data of DNA-DAPI complex in absence and presence of varying amount of $[Ch]_2[Mn]$ IL

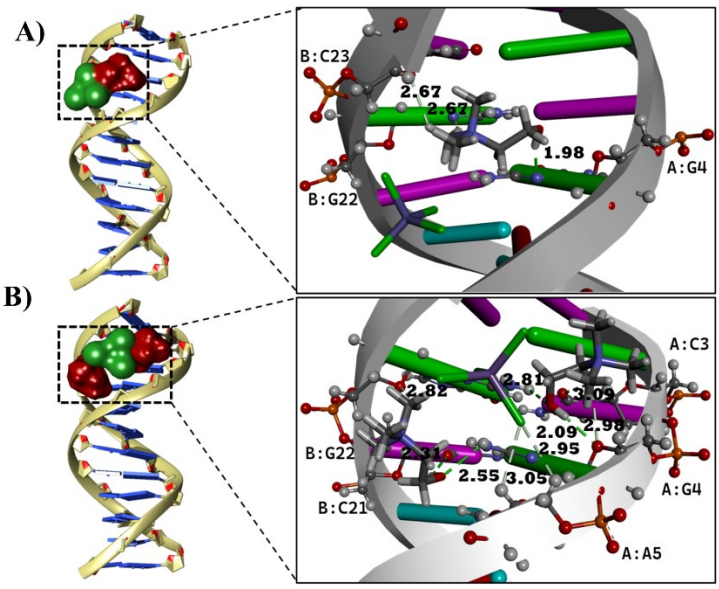

Figure S9: The 3D docking poses and interaction images of ct-DNA with (A) Fe-ChMIL and (B) Mn-ChMIL (bond distances are provided in Å).

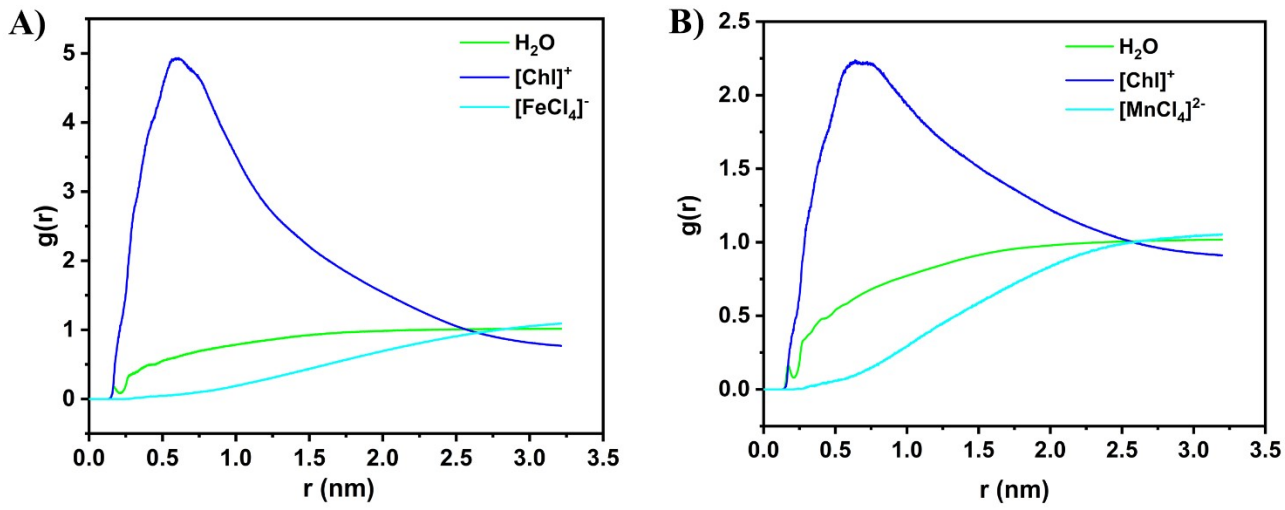

Figure S10: RDF plots of H_2O, $[Ch]^+$, and $[FeCl_4]^-$/ $[MnCl_4]^{2-}$ with respect to DNA in (A) DNA-[Ch][Fe] and (B) DNA-$[Ch]_2$[Mn] systems.

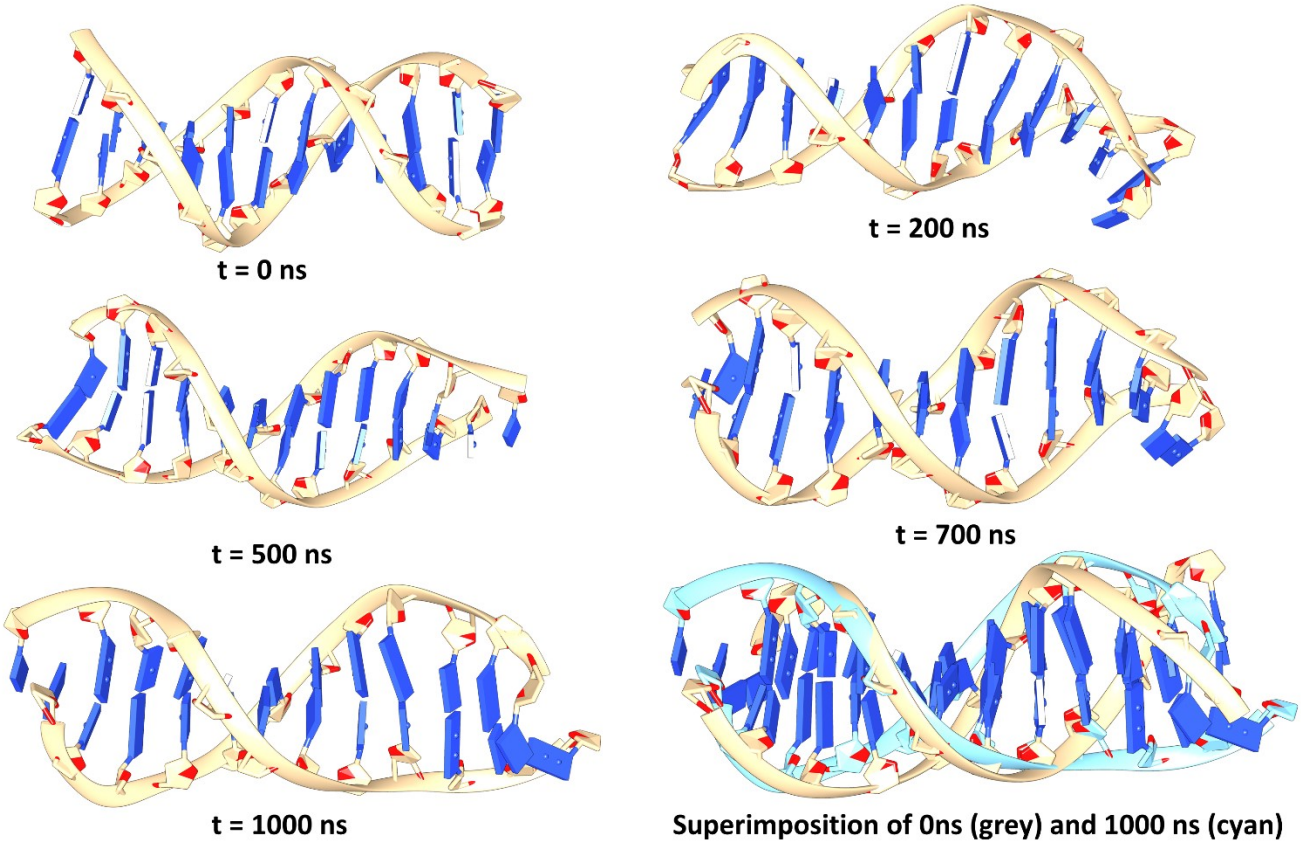

Figure S11: DNA conformations at different time instants (0, 200, 500, 700, and 1000 ns) and superimposition of structures at 0 ns and 1000 ns in $[Ch]_2[Mn]$ IL.

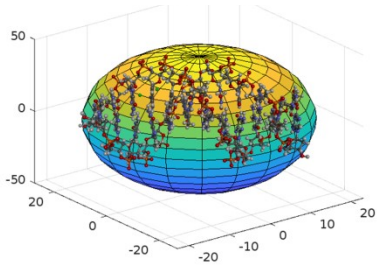

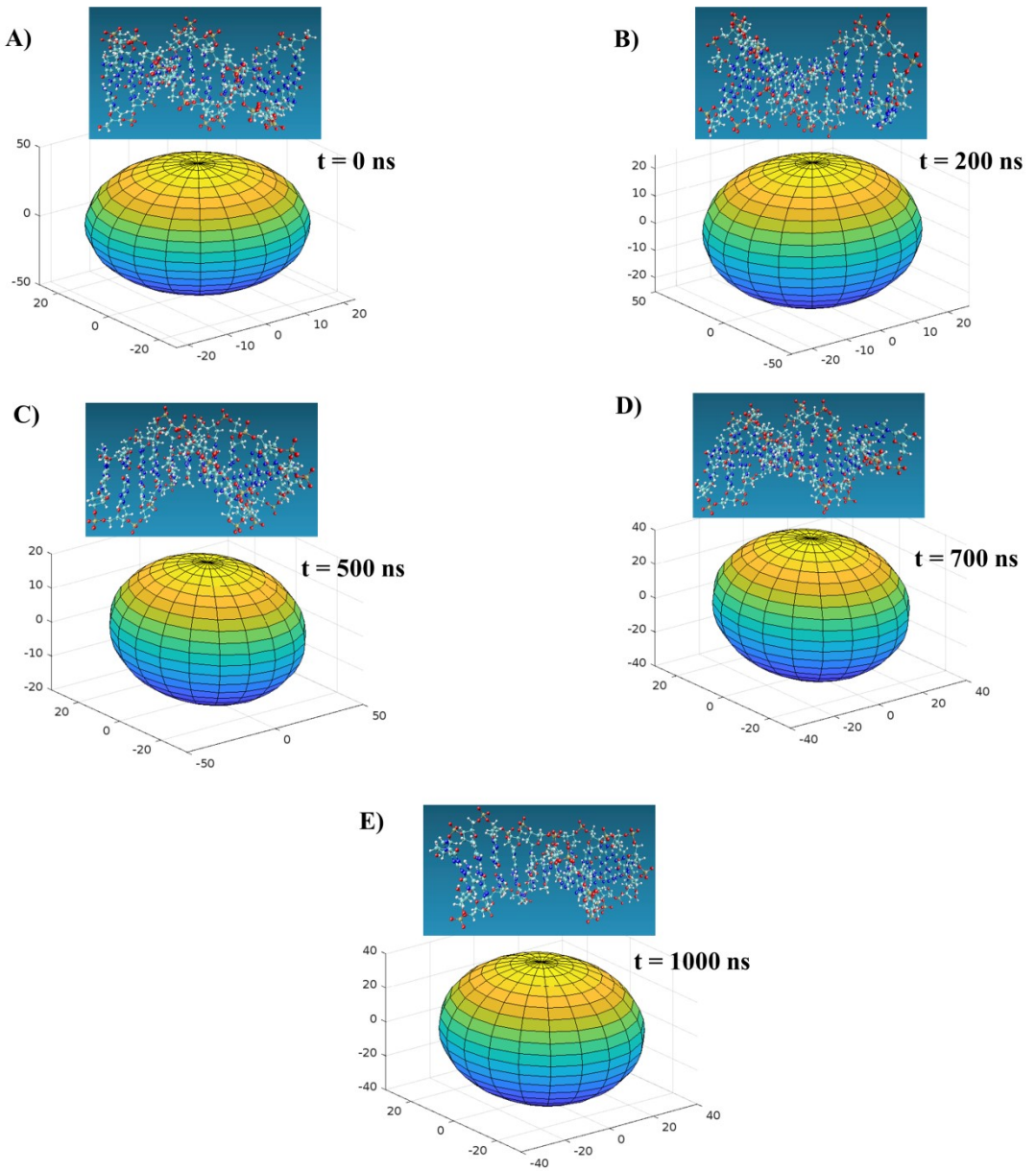

Figure S12: Illustrates the DNA volume as a 3D elliptical image for the DNA-$[Ch]_2[Mn]$ system at different time instants: 0 ns, 200 ns, 500 ns, 700 ns, and 1000 ns.

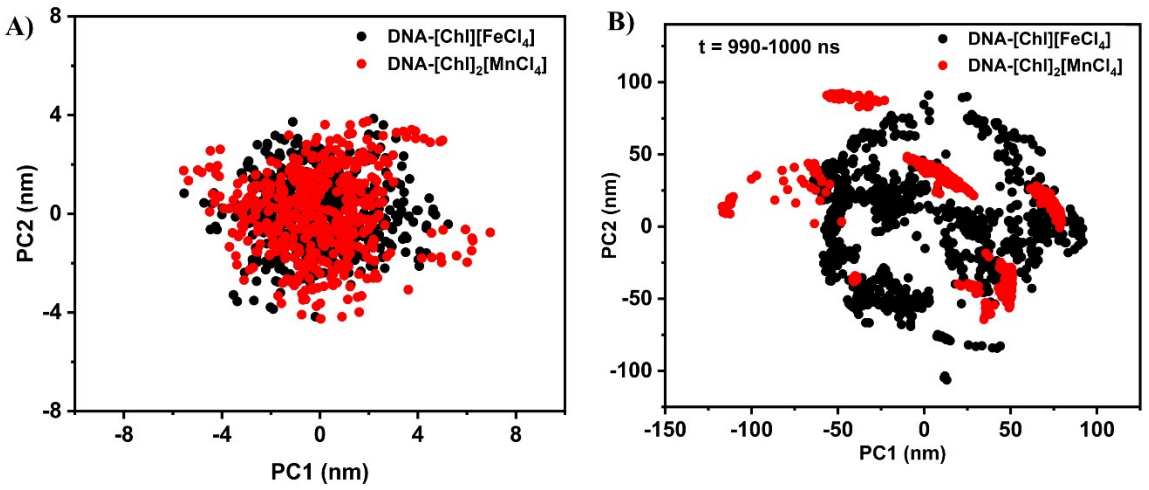

Figure S13: Principal component analysis of the DNA-[Ch][Fe] (black) and DNA-$[Ch]_2$[Mn] (red) simulation trajectories for the (A) first 10 ns (0-10 ns) and (B) last 10 ns (990-1000 ns).

References:

1. V. Hornak, R. Abel, A. Okur, B. Strockbine, A. Roitberg and C. Simmerling, Comparison of multiple Amber force fields and development of improved protein backbone parameters, *Proteins: Structure, Function, and Bioinformatics*, 2006, **65**, 712-725.
2. M. T. Panteva, G. M. Giambaşu and D. M. York, Force Field for Mg2+, Mn2+, Zn2+, and Cd2+ Ions That Have Balanced Interactions with Nucleic Acids, *The Journal of Physical Chemistry B*, 2015, **119**, 15460-15470.
3. A. K. Rappe, C. J. Casewit, K. S. Colwell, W. A. Goddard, III and W. M. Skiff, UFF, a full periodic table force field for molecular mechanics and molecular dynamics simulations, *Journal of the American Chemical Society*, 1992, **114**, 10024-10035.
4. K. Lindorff-Larsen, S. Piana, K. Palmo, P. Maragakis, J. L. Klepeis, R. O. Dror and D. E. Shaw, Improved side-chain torsion potentials for the Amber ff99SB protein force field, *Proteins*, 2010, **78**, 1950-1958.
5. S. A. Showalter and R. Brüschweiler, Validation of Molecular Dynamics Simulations of Biomolecules Using NMR Spin Relaxation as Benchmarks: Application to the AMBER99SB Force Field, *J. Chem. Theory Comput.*, 2007, **3**, 961-975.
6. V. Hornak, R. Abel, A. Okur, B. Strockbine, A. Roitberg and C. Simmerling, Comparison of multiple Amber force fields and development of improved protein backbone parameters, *Proteins*, 2006, **65**, 712-725.

7. O. Trott and A. J. Olson, AutoDock Vina: Improving the speed and accuracy of docking with a new scoring function, efficient optimization, and multithreading, *J. Comput. Chem.*, 2010, **31**, 455-461.
8. J. Eberhardt, D. Santos-Martins, A. F. Tillack and S. Forli, AutoDock Vina 1.2.0: New Docking Methods, Expanded Force Field, and Python Bindings, *J. Chem. Inf. Model.*, 2021, **61**, 3891-3898.
9. A. K. Ray, P. S. Sen Gupta, S. K. Panda, S. Biswal, U. Bhattacharya and M. K. Rana, Repurposing of FDA-approved drugs as potential inhibitors of the SARS-CoV-2 main protease: Molecular insights into improved therapeutic discovery, *Comput. Biol. Med.*, 2022, **142**, 105183.
10. S. K. Panda, P. S. Sen Gupta, S. Karmakar, S. Biswal, N. C. Mahanandia and M. K. Rana, Unmasking an Allosteric Binding Site of the Papain-like Protease in SARS-CoV-2: Molecular Dynamics Simulations of Corticosteroids, *J. Phys. Chem. Lett.*, 2023, **14**, 10278-10284.
11. H. R. Drew, R. M. Wing, T. Takano, C. Broka, S. Tanaka, K. Itakura and R. E. Dickerson, Structure of a B-DNA dodecamer: conformation and dynamics, *PNAS*, 1981, **78**, 2179-2183.
12. D. S. Biovia, Discovery Studio Modeling Environment. Dassault Syst. Release, San Diego, 2015, **4**.
13. L. A. H. v. d. Spoel., GROMACS 2021 Source Code. Zenodo, January 22, 2021.
14. H. J. C. Berendsen, J. P. M. Postma, W. F. van Gunsteren and J. Hermans, in *Intermolecular Forces: Proceedings of the Fourteenth Jerusalem Symposium on Quantum Chemistry and Biochemistry Held in Jerusalem, Israel, April 13–16, 1981*, ed. B. Pullman, Springer Netherlands, Dordrecht, 1981, DOI: 10.1007/978-94-015-7658-1_21, pp. 331-342.
15. U. Essmann, L. Perera, M. L. Berkowitz, T. Darden, H. Lee and L. G. Pedersen, A smooth particle mesh Ewald method, *The Journal of Chemical Physics*, 1995, **103**, 8577-8593.
16. B. Hess, H. Bekker, H. J. C. Berendsen and J. G. E. M. Fraaije, LINCS: A linear constraint solver for molecular simulations, *Journal of Computational Chemistry*, 1997, **18**, 1463-1472.
17. S. K. Panda, P. S. Sen Gupta, S. Biswal, A. K. Ray and M. K. Rana, ACE-2-Derived Biomimetic Peptides for the Inhibition of Spike Protein of SARS-CoV-2, *Journal of Proteome Research*, 2021, **20**, 1296-1303.

18. S. K. Panda, S. Saxena, P. S. S. Gupta and M. K. Rana, Inhibitors of Plasmepsin X Plasmodium falciparum: Structure-based pharmacophore generation and molecular dynamics simulation, *Journal of Molecular Liquids*, 2021, **340**, 116851.
19. B. R. Miller, III, T. D. McGee, Jr., J. M. Swails, N. Homeyer, H. Gohlke and A. E. Roitberg, MMPBSA.py: An Efficient Program for End-State Free Energy Calculations, *Journal of Chemical Theory and Computation*, 2012, **8**, 3314-3321.
20. R. Kumari, R. Kumar and A. Lynn, g_mmpbsa—A GROMACS Tool for High-Throughput MM-PBSA Calculations, *J. Chem. Inf. Model.*, 2014, **54**, 1951-1962.
21. R. Kulandaisamy, T. Kushwaha, A. Dalal, V. Kumar, D. Singh, K. Baswal, P. Sharma, K. Praneeth, P. Jorwal, S. R. Kayampeta, T. Sharma, S. Maddur, M. Kumar, S. Kumar, A. Polamarasetty, A. Singh, D. Sehgal, S. L. Gholap, M. B. Appaiahgari, M. R. Katika and K. K. Inampudi, Repurposing of FDA Approved Drugs Against SARS-CoV-2 Papain-Like Protease: Computational, Biochemical, and in vitro Studies.*Journal*, 2022, **13**, 877813.
22. C. Wang, D. A. Greene, L. Xiao, R. Qi and R. Luo, Recent Developments and Applications of the MMPBSA Method, *Front. mol. biosci*, 2018, **4**.
23. S. Genheden and U. Ryde, The MM/PBSA and MM/GBSA methods to estimate ligand-binding affinities, *Expert Opin. Drug Discov.*, 2015, **10**, 449-461.
24. T. Yang, J. C. Wu, C. Yan, Y. Wang, R. Luo, M. B. Gonzales, K. N. Dalby and P. Ren, Virtual screening using molecular simulations, *Proteins*, 2011, **79**, 1940-1951.
25. N. Homeyer and H. Gohlke, Free Energy Calculations by the Molecular Mechanics Poisson−Boltzmann Surface Area Method, *Mol. Inf.*, 2012, **31**, 114-122.
26. Z. Wang, X. Wang, Y. Li, T. Lei, E. Wang, D. Li, Y. Kang, F. Zhu and T. Hou, farPPI: a webserver for accurate prediction of protein-ligand binding structures for small-molecule PPI inhibitors by MM/PB(GB)SA methods, *Bioinformatics*, 2018, **35**, 1777-1779.
27. W. Humphrey, A. Dalke and K. Schulten, VMD: Visual molecular dynamics, *J. Mol. Graph.*, 1996, **14**, 33-38.
28. E. F. Pettersen, T. D. Goddard, C. C. Huang, G. S. Couch, D. M. Greenblatt, E. C. Meng and T. E. Ferrin, UCSF Chimera—A visualization system for exploratory research and analysis, *J. Comput. Chem.*, 2004, **25**, 1605-1612.